高等学校化学学报
CHEMICAL JOURNAL OF CHINESE UNIVERSITIES
综合评述

拉曼成像技术的前沿进展及与聚集体科学的交叉研究

李雨婷，罗　亮
（华中科技大学生命科学与技术学院，武汉 430074）

摘要　拉曼成像作为一种分子光谱技术，凭借其出色的特异性和高分辨率，在生命科学等领域得到了广泛的研究与应用. 然而其发展仍面临信号微弱、采集速度慢及穿透深度不足等挑战. 近年来，聚集科学的快速发展为解决拉曼成像的局限性提供了新思路. 聚集诱导发光(AIE)材料在聚集状态下会表现出增强的信号，有望弥补拉曼信号固有的微弱性. 本文综合评述了拉曼成像技术的前沿进展及其与聚集科学交叉研究的现状，重点阐述了通过分子工程构建AIE-拉曼双响应探针的策略，以实现荧光定位与拉曼定量之间的功能互补，从而显著提高检测的灵敏度和特异性. 这些探针在肿瘤手术导航、耐药菌诊疗及细胞器动态监测等应用中已展现出单细胞分辨率和高时空准确性. 我们还分析了该领域面临的挑战，如生物安全性和分子设计的复杂性，并对未来的发展方向进行了展望，包括智能响应探针、人工智能辅助分析以及多模态融合平台. 拉曼成像与AIE的融合将为医学成像等领域的突破性发展指明新方向.

关键词　拉曼成像；探针；聚集体；聚集诱导发光
中图分类号　O632　　**文献标志码**　A　　doi：10.7503/cjcu20260008

Cutting-edge Advances in Raman Imaging Technology and Its Interdisciplinary Research with Aggregate Science

LI Yuting, LUO Liang*
(*College of Life Science and Technology*, *Huazhong University of Science and Technology*, *Wuhan* 430074, *China*)

Abstract　Raman imaging, as a molecular spectroscopy technique, has been widely studied and applied in research fields such as life sciences and food safety due to its excellent specificity and high resolution. However, its development still faces challenges such as weak signals, slow acquisition speed, and insufficient penetration depth. In recent years, the rapid development of aggregate science has provided new insights for addressing these limitations. Aggregation-induced emission (AIE) materials exhibit enhanced signals in the aggregated state, which may compensate for the inherent weak Raman signals. This article reviews the cutting-edge progress of Raman imaging technology and its current status in cross-disciplinary research with aggregate science, emphasizing the strategy of constructing AIE-Raman dual-responsive probes through molecular engineering to achieve functional complementarity between fluorescence localization and Raman quantification, thereby significantly improving detection sensitivity and specificity. These probes have demonstrated single-cell resolution and high spatiotemporal accuracy in applications such as tumor surgical navigation, diagnosis and treatment of drug-resistant bacteria, and dynamic monitoring of organelles. We also analyze the bottlenecks in this field, such as biological safety and the complexity of molecular design, and outline the future development directions, including intelligent responsive

收稿日期：2026-01-01. 网络首发日期：2026-02-22.
联系人简介：罗　亮，男，博士，教授，主要从事有机高分子功能材料的设计制备与在生物医学中的应用方面的研究.
E-mail：liangluo@hust.edu.cn
基金项目：国家自然科学基金(批准号：52325304)资助.
Supported by the National Natural Science Foundation of China(No.52325304).

probes, artificial intelligence-assisted analysis, and multimodal fusion platforms. The integration of Raman imaging and AIE sheds new light in the field of medical imaging.

Keywords Raman imaging; Probe; Aggregate; Aggregation-induced emission(AIE)

1 Introduction

The Raman scattering effect refers to the inelastic scattering of light resulting from interactions between photons and molecules[1]. When photons collide with molecules and exchange energy, the frequency of the scattered light shifts relative to the incident light. This frequency shift reflects changes in the vibrational and rotational energy levels of the molecules[2,3]. Owing to this vibrational fingerprint characteristic, Raman spectroscopy has become a pivotal tool for elucidating chemical structures[4]. As an optical method that requires no exogenous labeling, Raman spectroscopy enables label-free detection based on the intrinsic molecular vibrations of analytes[5,6]. This not only simplifies sample preparation but also circumvents issues associated with fluorescent dyes, such as potential toxicity, photobleaching, and limited photostability[7]. Furthermore, the narrow spectral bandwidth of Raman signals allows for the discrimination of molecules with similar chemical structures, forming a critical foundation for highly selective analysis[8]. Advances in hardware technologies including lasers, filters, and single-photon detectors, have substantially improved the signal-to-noise ratio and acquisition efficiency of Raman systems, laying a solid groundwork for the progression of Raman imaging[9,10]. In imaging mode, when combined with the spatial resolution of microscopic optical systems, Raman technology facilitates structural and compositional analysis at the sub-micron scale, providing high-spatial-resolution chemical mapping for fields such as life sciences, materials science, and pharmaceutical analysis[11—13].

Early Raman-based imaging modalities primarily relied on confocal Raman microscopy. This technique involves point-scanning the sample with excitation light, recording complete vibrational spectra at each pixel, and reconstructing spatial information from the spectral data to generate two- or three-dimensional chemical composition maps[14,15]. It offers high spatial resolution, strong spectral specificity, and the capability for quantitative analysis in complex systems, making it a valuable tool for studying chemical reaction kinetics, cellular metabolism, and material structures[16]. However, the point-scanning nature of confocal Raman microscopy often results in relatively slow imaging speeds, limiting its applicability for real-time monitoring of rapid dynamic processes[17]. To address this limitation, various signal enhancement and acceleration strategies have been developed. A prominent example is surface-enhanced Raman scattering(SERS), which leverages localized surface plasmon resonances generated by metallic nanostructures to amplify Raman signals by several orders of magnitude, therefore enabling highly sensitive detection even down to the single-molecule level[18]. Concurrently, the rapid development of coherent Raman imaging techniques has provided crucial pathways to overcome the speed constraints of conventional scanning. Coherent anti-Stokes Raman scattering(CARS) and stimulated Raman scattering(SRS) utilize coherent optical fields to enhance vibrational signals, significantly boosting signal levels and suppressing background noise[19—22]. These techniques can achieve video-rate imaging speeds, making them suitable for real-time observation of living tissues and fast biological processes. Moreover, emerging technologies such as wide-field Raman imaging, compressive sensing Raman imaging, and deep learning-assisted spectral reconstruction have further accelerated Raman data acquisition and processing, enabling high-throughput, multi-dimensional Raman analysis[23—27]. Overall, the evolution of Raman imaging is shifting from traditional high-spectral-resolution scanning toward high-speed, low-photodamage, real-time, and dynamic imaging modalities.

Despite the continuous refinement of Raman imaging technologies, their development remains

constrained by several challenges. First, the inherently small Raman scattering cross-section leads to weak intrinsic signals, necessitating long acquisition times to achieve sufficient signal-to-noise ratios. This not only limits imaging speed but also increases risks such as photobleaching and thermal effects, which are particularly problematic in biological tissues[28]. Second, there exists a fundamental trade-off among high spectral resolution, broad spectral range, and high acquisition speed. Rapid imaging often relies on spectral compression or reduced sampling, which inevitably compromises spectral detail and thereby affects the accuracy of compositional discrimination[29,30]. More importantly, Raman imaging exhibits limited penetration depth in thick tissues. Significant scattering and absorption in biological samples attenuate the signal, restricting the effective imaging depth of Raman techniques compared to established methods such as multiphoton fluorescence microscopy[31]. Furthermore, although high-speed coherent Raman methods markedly improve imaging efficiency, their system complexity, high costs, and stringent requirements for laser source stability hinder widespread adoption in conventional laboratory and clinical settings[32]. Therefore, Raman spectroscopic imaging urgently requires the integration of novel technical approaches to overcome these existing limitations.

Aggregation-induced emission (AIE), a landmark concept in aggregate science, was first proposed in 2001 by Prof. Tang and coworkers[33,34]. In stark contrast to aggregation-caused quenching (ACQ) materials, AIE materials exhibit weak emission in the monomeric state while demonstrating significantly enhanced fluorescence intensity upon aggregation or in the solid state[35]. Representative AIE chromophores such as tetraphenyl ethylene (TPE), characterized by their non-planar propeller-shaped configurations, exemplify the transition from molecular behavior to emergent aggregate properties, establishing a research paradigm spanning from molecular design to aggregate regulation[36,37].

The introduction of the AIE concept has not only overcome the critical limitation of ACQ in solid-state luminescence but also opened new avenues for constructing high-performance functional materials through precise control of molecular aggregation[38]. In the realm of biosensing and bioimaging, AIE materials have demonstrated tremendous potential owing to their high emission efficiency in aggregated states, exceptional photostability, and minimal background interference[39,40]. With ongoing research advancements, AIE systems have expanded from classical structures like TPE and triphenylamine (TPA) to sophisticated architectures featuring donor-acceptor (D-A) configurations, as well as complex systems exhibiting excited-state intramolecular proton transfer (ESIPT) or twisted intramolecular charge transfer (TICT) characteristics[41—43]. These developments have substantially broadened the scope of luminescence modulation and application boundaries. AIE-based probes have shown outstanding performance in detecting various analytes, including metal ions, reactive oxygen species, gaseous signaling molecules, pH variations, enzymatic activities, and disease biomarkers[44—46]. Particularly noteworthy is the progress in second near-infrared window (NIR-II) AIE probes, which have considerably improved tissue penetration depth and spatial resolution for *in vivo* imaging[47].

In recent years, the integration of AIE with Raman imaging has emerged as a prominent research focus. Innovative strategies include the development of AIE-Raman dual-modal probes and aggregation-enhanced Raman signal systems (Fig.1). These approaches provide

Fig. 1 Research progress of Raman imaging and its integration with aggregate science

powerful tools for tumor imaging, drug delivery, and real-time monitoring of live cell metabolism. The synergy between AIE and Raman imaging effectively compensates for the inherent weaknesses of Raman imaging, such as weak signals and slow acquisition speeds, while offering novel design strategies for multimodal imaging platforms and high-sensitivity analytical techniques[48]. This convergence represents a significant future direction for biomedical imaging applications.

2 Core Technologies and Development of Raman Imaging

2.1 Spontaneous Raman Imaging

Spontaneous Raman Imaging is a spectroscopic technique based on molecular inelastic scattering, whose principle originates from the interaction of photons with molecular vibrational modes. When a monochromatic laser irradiates a sample, the vast majority of photons undergo elastic Rayleigh scattering, while only about one in 10^8 events produces Raman scattering[49,50]. This process reveals vibrational information of chemical bonds through changes in molecular polarizability, generating molecule-specific "fingerprint spectra". In biological systems, approximately 90% of spontaneous Raman bands are concentrated in the characteristic region of 400—1800 cm^{-1}, with the remainder distributed in the C—H/O—H stretching vibration region spanning 2700—3300 cm^{-1}, allowing precise reflection of the composition and conformational changes of major biomacromolecules such as proteins, lipids, and nucleic acids[51]. Unlike SERS which requires metal nanostructures for enhancement, spontaneous Raman can directly detect the intrinsic biochemical information of samples without exogenous labels or substrates[52].

In cellular and tissue research, spontaneous Raman imaging has demonstrated unique application value. At the cellular level, this technique can track organelle dynamics and interactions in real-time, monitor molecular redistribution during mitosis, and achieve precise identification of physiological and pathological processes such as stem cell differentiation and apoptosis through spectral fingerprint analysis[53,54]. At the tissue level, spontaneous Raman is widely used for tumor pathological diagnosis, such as detecting 5, 6-dihydroxyindole metabolites in melanoma, distinguishing pancreatic cancer from pancreatitis, and analyzing cholesterol metabolism abnormalities in colon cancer[49,55]. Recent studies have further expanded its application scenarios. One hundred percent accuracy has been achieved in diagnosis of rheumatoid arthritis *via* intelligent two-dimensional biopsy through scanning the skin of affected joints[56]. Micro-spectral analysis of brain tissues from epilepsy model animals in field of neuroscience has revealed abnormal expressions of glial fibrillary acidic protein (GFAP)[57]. Additionally, the spatial distribution of hypoxia-inducible factor-1 (HIF-1) and programmed death-ligand 1(PD-L1) has been mapped in research related to the tumor microenvironment[49]. These applications are all based on the label-free analytical capability of spontaneous Raman for tissue biochemical composition, enabling the revelation of disease-related macromolecular structural changes at the molecular level.

However, inherent defects in spontaneous Raman imaging significantly constrain its clinical translation. The most prominent limitation is its extremely weak signal intensity, leading to a low signal-to-noise ratio. This often necessitates optimization of laser power and integration time. High-quality spectral acquisition at a single point can take about 100 ms, and imaging a 10 mm×10 mm tissue sample can take up to 3 h, severely limiting the monitoring of dynamic processes[49].

2.2 Enhanced Raman Imaging Techniques

While traditional spontaneous Raman imaging can provide molecule-specific information, its inherent low scattering cross-section leads to insufficient sensitivity and slow imaging speed, making it difficult to meet the demands of biomedical research for high spatiotemporal resolution and dynamic monitoring. In recent years,

various novel Raman-enhanced imaging techniques have significantly improved detection sensitivity and functional specificity by introducing strategies such as plasmon coupling, gap resonance, stimulus-response, and molecular engineering, opening new avenues for live-cell analysis, drug delivery monitoring, and clinical diagnosis.

2.2.1 SERS Imaging SERS imaging technology overcomes the inherent weakness of spontaneous Raman signals by utilizing localized surface plasmon resonance generated by noble metal nanostructures, which can enhance the Raman signals of adsorbed molecules by up to 10^{14}-fold[58,59]. The enhancement mechanism primarily stems from the synergistic effect of electromagnetic field enhancement and chemical enhancement [Fig.2(A) and (B)][60—62]. SERS not only overcomes the drawback of weak signals but also offers advantages such as resistance to photobleaching, narrow spectral bandwidth, and excellent multi-channel detection capability[63,64].

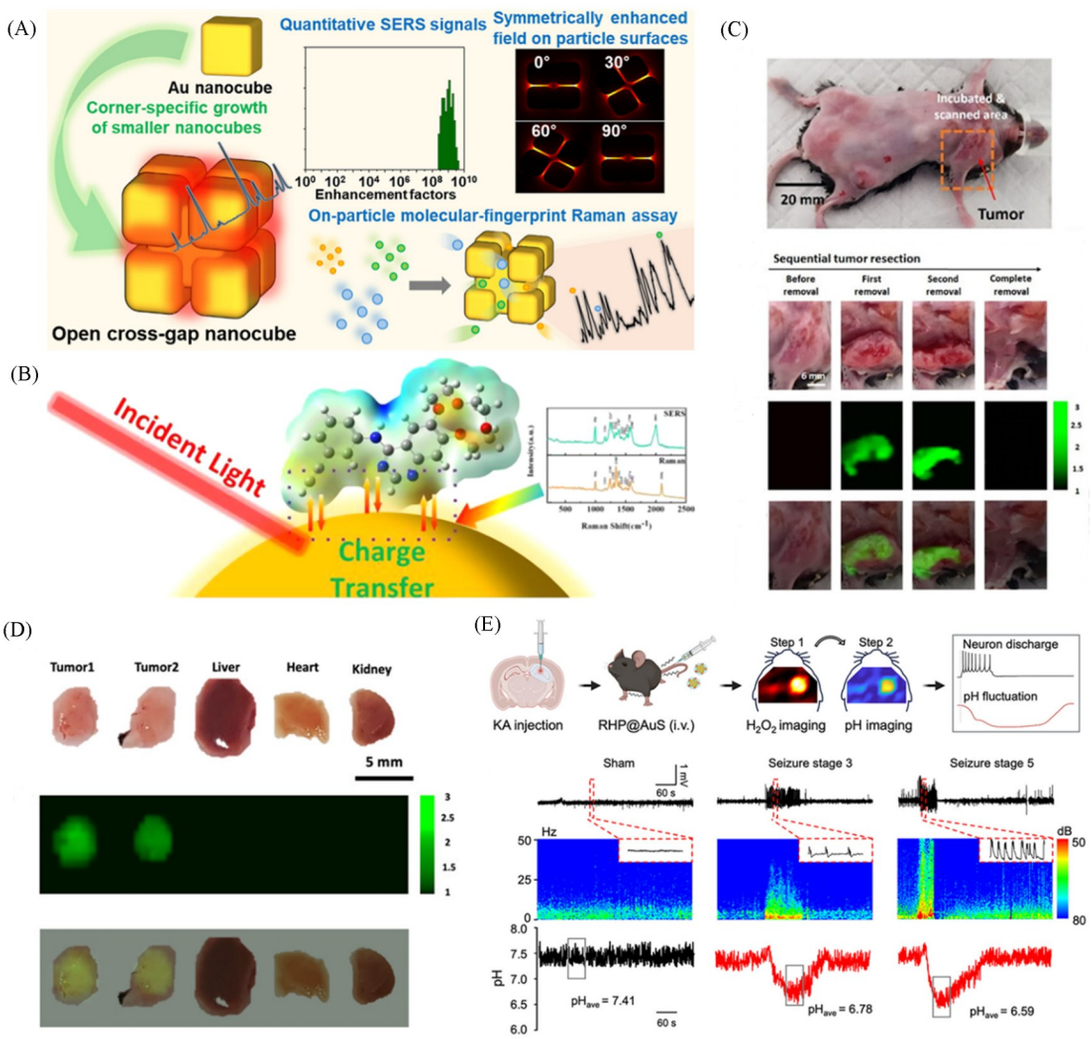

Fig. 2 Two enhancement principles of SERS: diagrams illustrating the electromagnetic field enhancement principle[61] (A) and the chemical enhancement principle[62] (B), utilizing "sugar nanoparticles" to achieve real-time intraoperative imaging and complete resection of the spontaneous breast cancer model in mice[58] (C), the images obtained by using ratio-type Raman probes on tumor tissues and control tissues[58] (D), imaging pH fluctuations with RHP@AuS in KA model mice[78] (E)

(A) Copyright 2024, American Chemical Society; (B) Copyright 2021, American Chemical Society; (C, D) Copyright 2024, Wiley-VCH; (E) Copyright 2025, Wiley-VCH.

The evolution of SERS substrate design directly determines the limits of imaging performance. Early studies primarily relied on spherical gold nanoparticles[65]. To overcome their limitations, researchers have developed anisotropically shaped structures[66,67] and three-dimensional structures such as hollow nanoshells and core-satellite assemblies[68]. Notably, innovative structures like Gap-Enhanced Raman Tags (GERTs) achieve controllable "hot spots" while maintaining physical stability, balancing the needs for sensitivity and biocompatibility[69]. Nanoprobe engineering further enhances SERS imaging performance. A typical SERS nanoprobe consists of four components: a plasmonic substrate, Raman labeling compounds (RLCs), a protective layer, and a biological targeting ligand[70]. While traditional organic dyes can offer resonance enhancement, they often suffer from photobleaching and spectral overlap[71]. In contrast, bioorthogonal RLCs can shift characteristic peaks to the "biological silent region" (1800—2800 cm^{-1}), effectively avoiding background interference[72—75]. The design of the protective layer (*e.g.*, PEGylation) and the conjugation method of targeting ligands are also crucial[76,77]. For example, "glyconanoparticles" formed by anchoring hyaluronic acid (HA) onto SERS particle surfaces *via* liposomes exhibit significantly higher affinity for the CD44 receptor than direct chemical conjugation, successfully enabling real-time intraoperative imaging and complete resection in a mouse model of spontaneous breast cancer[Fig.2(C)][58].

The biological applications of SERS imaging span from *in vitro* diagnostics to *in vivo* precision medicine. In oncology, ratio imaging strategies, by simultaneously injecting targeted and non-targeted probes, can precisely delineate tumor boundaries[Fig.2(D)], achieving a detection limit for residual intraoperative lesions as low as the femtomolar level[58]. The recently developed tandem dual-ratio SERS probe RHP@AuS can cross the blood-brain barrier and monitor real-time dynamic fluctuations of brain tissue pH during epileptic seizures [Fig. 2 (E)][78]. Furthermore, Surface-Enhanced Hyper-Raman Scattering (SEHRS), as a two-photon excitation technique combined with multivariate data processing methods like principal component analysis, enables high spatial resolution imaging within the pH range of 4—7. 5 in intracellular vesicle systems[79].

The precise control of nanoparticle aggregation behavior in SERS technology, such as inducing the formation of uniform, high-density "hot spots" through external field driving or interfacial chemistry, is highly aligned with the core concept of aggregate science, which constructs high-performance functional materials through controlled molecular or nanoscale assembly. This active design and optimization of the "aggregate state" not only provides key ideas for improving the sensitivity and reproducibility of SERS probes but also lays the foundation for subsequent integration with AIE strategies. For example, future work could explore the co-assembly of AIE luminogens (AIEgens) with SERS-active nanostructures to construct dual-responsive probes that combine aggregation-enhanced luminescence and plasmon-enhanced Raman signals, achieving functional complementarity and performance multiplication.

2.2.2 TERS Imaging Tip-Enhanced Raman Scattering (TERS) imaging technology integrates scanning probe microscopy with SERS. By utilizing the localized electromagnetic field enhancement effect generated at the tip of a metal probe, it overcomes the optical diffraction limit, enabling chemical-specific analysis at the nanoscale[80]. Key factors affecting TERS resolution include sampling step size, instrumental drift, probe tip size, and geometry. Its spatial resolution has progressively improved from an initial 50—100 nanometers to the sub-nanometer level. Achieving this resolution breakthrough relies on optimizing probe fabrication techniques, employing atomically sharp probes, and developing environments like ultra-high vacuum low-temperature(UHV-LT) systems[81—83].

TERS demonstrates significant potential in nanoscale chemical analysis. In the study of two-dimensional materials, TERS has successfully revealed defect distribution, local strain, and doping heterogeneity in graphene[81]. Hwang and Jhe[82] further note that TERS can not only probe defect structures in transition metal

dichalcogenides (TMDCs) but also achieve optical manipulation of dark excitons by tuning gap plasmons. Biomaterial analysis is another important application. Mrđenović *et al.*[84] used TERS for label-free chemical imaging of live cell membranes, achieving a spatial resolution of 2.5 nanometers under ambient conditions and successfully distinguishing nanodomains enriched with different components [Fig. 3(A)]. Compared to diffraction-limited confocal Raman imaging, TERS revealed the heterogeneous distribution of membrane components at the nanoscale [Fig. 3(B)]. Additionally, TERS can be employed to investigate catalytic and surface chemical mechanisms, for example, by combining DFT calculations to study the selective adsorption of CO_2 on $SrTiO_3$ photocatalyst surfaces[85], and can also monitor plasmon-driven photocatalytic reactions *in situ*[82].

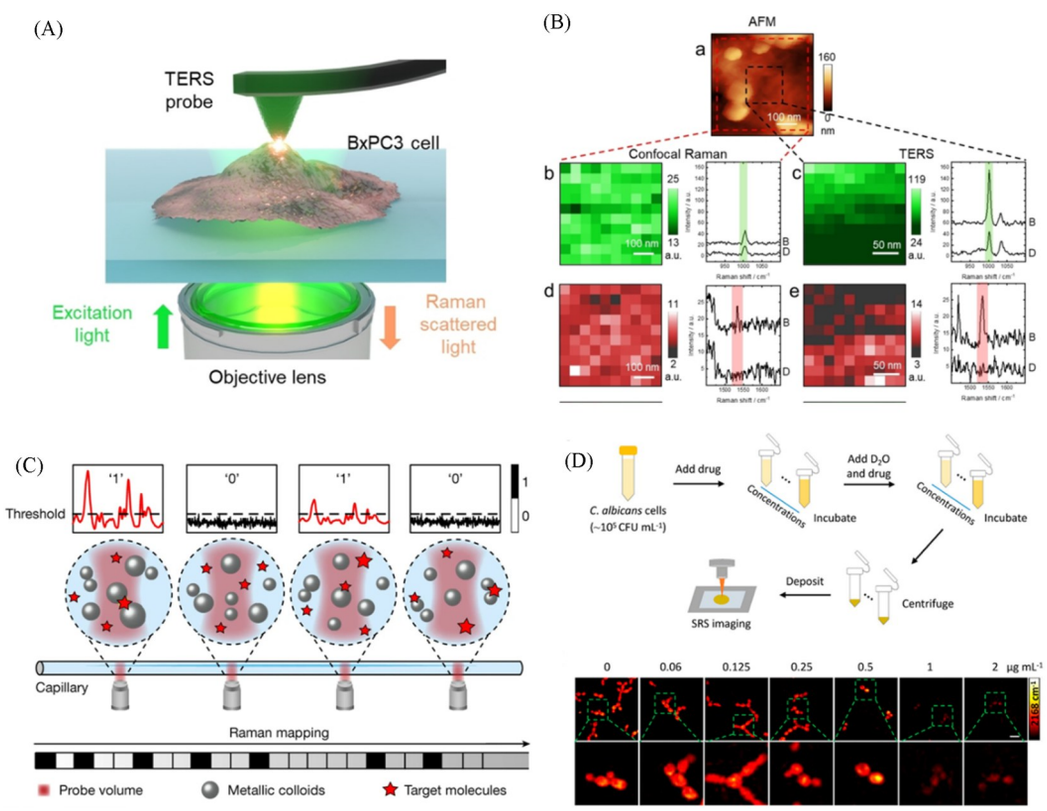

Fig. 3 TERS images of the living cell membrane[84](A), compared with Confocal Raman, TERS reveals the heterogeneous distribution of membrane components at the nanoscale[84](B), schematic of dCERS[86](C), and the schematic diagram of rapid AFST using SRS metabolic imaging and a bacterial SRS image based on C—D peaks[87](D)

(A, B) Copyright 2022, Wiley-VCH; (C) Copyright 2024, Springer Nature; (D) Copyright 2023, American Chemical Society.

The nanoscale and even sub-nanoscale spatial resolution provided by TERS offers an unprecedented tool for *in situ* investigation of aggregate state formation processes, microstructures, and physicochemical properties at the molecular level. This is crucial for deepening the understanding of fundamental AIE mechanisms. For example, TERS could be employed to observe in real time the transition of AIE molecules from a dispersed to an aggregated state under specific stimuli, directly characterize intermolecular interactions and arrangements within aggregates, or correlate the enrichment of AIE probes in organelles with the local nano-environment. Therefore, TERS is not only a powerful tool for material characterization but also holds future promise as a key bridge connecting molecular design, aggregate state regulation, and macroscopic optical properties, thereby advancing AIE-Raman interdisciplinary research to more microscopic and

fundamental levels.

2.2.3 Other Enhancement Techniques Plasmon-enhanced resonance Raman strategies represent an important direction for ultra-sensitive imaging. Surface-enhanced resonance Raman scattering (SERRS) achieves a signal enhancement of 6—8 orders of magnitude by synergistically coupling molecular resonance with the LSPR of metal nanostructures. Studies show that tuning the absorption peak of azobenzene-based molecules to the visible region at 415 nm and precisely matching it with the LSPR peak of silver-core gold-shell nanoparticles (Ag@AuNPs) at 530 nm and the excitation wavelength at 532 nm can produce selective enhancement for C—N bond vibrations, achieving single-molecule level detection limits. This core-shell structure design not only retains the high electromagnetic field enhancement properties of silver but also improves biocompatibility and chemical stability through the gold shell. The core-shell thickness can be precisely tuned for optimal spectral overlap, with 530 nm resonant particles exhibiting the strongest enhancement under 532 nm excitation. Density functional theory calculations confirm that resonant excitation leads to intramolecular charge redistribution. Specifically, the C—N bond vibrational modes at both ends of the azo group receive maximum enhancement, while the tertiary amine C—N bond near the nanoparticle surface further contributes to synergistic amplification through chemical enhancement mechanisms[88].

Gap-enhanced resonance Raman tags (GERRTs) push the enhancement effect to new heights through a unique core-shell-molecule sandwich structure. This technology embeds the near-infrared resonant dye IR-780 between a petal-like gold core and a silver shell, utilizing multiple "hotspots" and core-shell coupling effects to boost Raman intensity by three orders of magnitude compared to traditional gap-enhanced tags. The strong absorption peak of IR-780 perfectly matches the 785 nm excitation laser, producing resonance Raman effects. The petal-like gold core provides a large molecular loading surface area and abundant nanogaps, while the silver shell acts both as a protective layer preventing dye leakage and further enhances the signal due to silver's excellent SERS activity. This design achieves single-nanoparticle level detection sensitivity, enabling high-speed live-cell imaging with ultra-short exposure time and low laser power, significantly reducing phototoxicity and supporting time-lapse monitoring for up to 8 h[89].

Stimulus-responsive resonance Raman scattering (SRRRS) imaging converts molecular recognition events directly into enhanced Raman signals, breaking the sensitivity limit of traditional optical probes. This technology utilizes the β-lactamase-catalyzed ring-opening reaction of nitrocefin, whose product absorption red-shifts to 480 nm, generating resonance with 633 nm excitation light and achieving a 2—3 order of magnitude signal enhancement. By immobilizing 4-mercaptophenylboronic acid on a gold nanobase to capture bacteria, the dynamic activity of β-lactamase can be monitored in real-time at the single-cell level, achieving ultra-sensitive detection of 10^2 cfu/mL. Studies found that β-lactamase activity in drug-resistant bacteria first appears at the bacterial poles, consistent with polar distribution of protein translation and cellular stress response mechanisms. An antibiotic breakpoint library established based on this allows susceptibility screening of *Pseudomonas aeruginosa* against 14 antibacterial drugs within 3 h, with clinical validation accuracy reaching 93%, significantly faster than traditional culture methods[90].

Specialized resonance Raman probe design achieves functional-specific imaging through molecular engineering. The azo-based resonance Raman pH probe (LysoAzo-pH) introduces a cyano electron-withdrawing group and a methoxy electron-donating group onto the azobenzene backbone, red-shifting the absorption peak to 495 nm. Simultaneously, it effectively quenches fluorescence background using the non-radiative transition of azobenzene, achieving a Raman enhancement factor of 10^3. This probe is highly sensitive to fingerprint vibrational changes caused by N=N bond cleavage and C—N bond formation during protonation/deprotonation reactions, the disappearance of the 1364 cm^{-1} peak and the blue shift of the 1414 cm^{-1} peak,

and it is capable of resolving lysosomal acidification processes with <0.2 pH unit differences. In autophagy studies, this method clearly revealed the spatial distribution changes of lysosomal pH in HeLa cells decreasing from 5.6±0.4 to 4.8±0.3 under starvation conditions, providing a new chemical imaging tool for cell metabolism research[91].

2.2.4 New Types of Raman Imaging Techniques Addressing the challenge of signal irreproducibility in SERS at ultra-low concentrations, the dCERS technology developed by Bi *et al.*[89] adopts a revolutionary digital counting approach. By binarizing each acquired spectrum as "positive/negative", counting the proportion of positive voxels, and utilizing the Poisson distribution for statistical quantification, this method theoretically avoids intensity fluctuations caused by uneven electromagnetic hotspots and molecular orientation, ensuring statistically uniform enhancement probability in colloidal suspension systems. Experiments confirm its universal quantitative capability for various molecules including proteins, nucleic acids, metabolites, and dyes, achieving single-molecule level detection limits. Compared to classical SERS, the quantitative error of dCERS is controllable and can be reduced by increasing acquisition time. It provides a standardized technical framework for clinical screening of trace biomarkers and is currently being integrated with the metabolomics technology "SERSome" to enhance early cancer diagnostic efficacy[Fig.3(C)][86].

Furthermore, SRS microscopy has catalyzed a series of novel Raman imaging methods, greatly expanding their application boundaries in precision medicine, drug screening, and biochemical analysis. For example, the rapid antifungal susceptibility testing(AF ST) method developed by Chen *et al.*[87] combines SRS metabolic imaging with heavy water(D_2O) probes, reducing detection time from 24 h to 48 h required by traditional methods to 4 h. By monitoring the formation rate of C—D bonds in single fungal cells, this technology discovered unique response patterns. Amphotericin B inhibits metabolism while azole drugs stimulate metabolism, achieving 100% classification consistency. A review by Hong *et al.*[87] further points out that this D_2O-SRS strategy can dynamically track the synthesis of biomacr omolecules like lipids, proteins, and nucleic acids, providing a high-throughput platform for biomarker discovery in cancer, infectious diseases, and metabolic syndrome[Fig. 3(D)].

3 Integration of Raman Imaging and Aggregate Science

3.1 Aggregated Materials as High-performance Raman Probes

The cross-interaction between aggregate science and Raman imaging provides a novel paradigm for constructing high-density, highly uniform "hot spot" structures through the active regulation of molecular/nanoscale assembly behavior, significantly enhancing the sensitivity, reproducibility, and biological applicability of probes. Its core scientific advantage lies in the controllability of the aggregation formation process, which enables the precise construction of localized electromagnetic field enhancement, while the stability of the aggregated state ensures reliable Raman signal output in complex biological environments.

In nanoparticle aggregation systems, controllability is manifested through the synergistic regulation of external field driving and interfacial chemistry. Park *et al.*[92] employed surface acoustic waves(SAW) to induce the centripetal aggregation of 50 nm silver nanoparticles(AgNPs) during droplet evaporation, avoiding the random coffee-ring effect and forming dense aggregates of approximately 2200 particles/μm^2 with uniformly distributed nano-gaps of approximately 1.5 nm. This dynamic assembly process achieved a detection limit for dopamine of 4.28 nmol/L with a linear correlation coefficient of 0.99[Fig.4(A)]. This active aggregation strategy not only increases hot spot density but also maintains droplet height through hydrophobic surface modification, ensuring nano-gaps remain intact during assembly, thereby addressing the challenge of non-uniform hot spots in traditional self-assembly. Similarly, the nano-aggregate-embedded beads(NAEBs)

developed by the Fong team employ chemically induced aggregation of AuNPs followed by *in situ* encapsulation within a SiO_2 shell[Fig.4(B)], solidifying the chemically enhanced "hot spots" into a stable core-shell structure. This design leverages strong plasmonic coupling when the AuNPs spacing is <20 nm, while the silica shell isolates the structure from external molecular interference, enabling a detection limit of 2000 CFU/mL for single-cell Salmonella detection, with stable recovery rates of 90%—110%. The encapsulation strategy for aggregates provides physical protection for the hot spot structure, maintaining signal stability even under shear forces within microfluidic chips, which is key to transforming dynamic aggregates into functional probes[93].

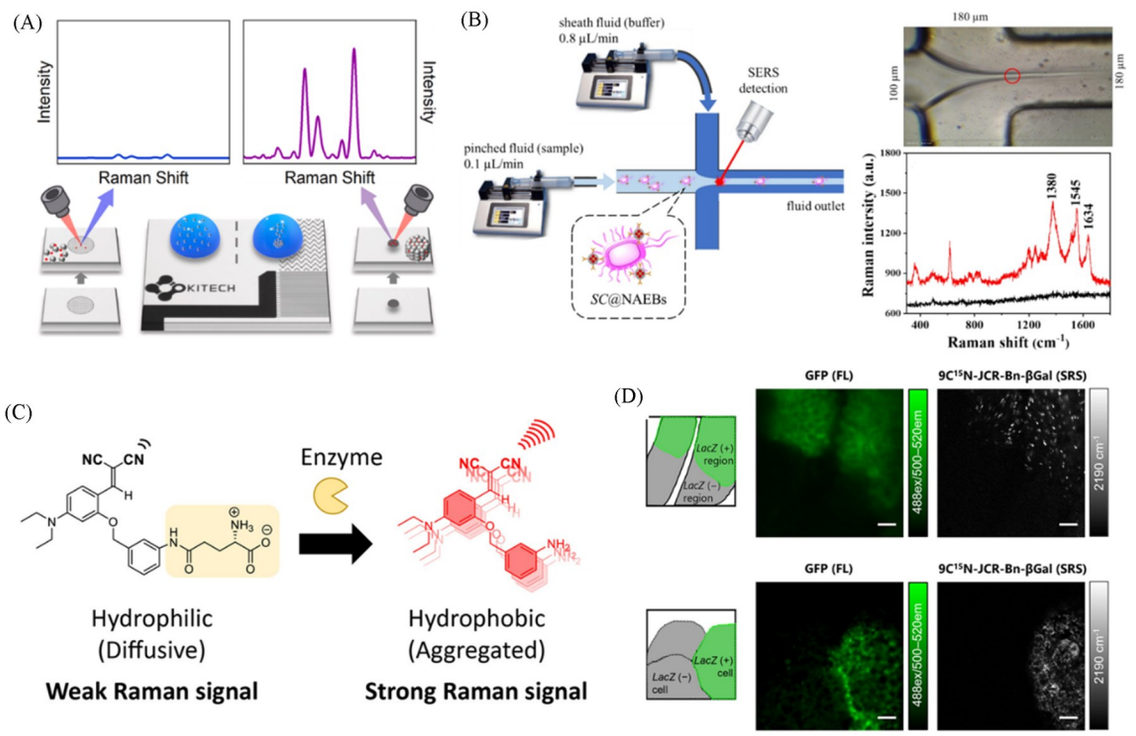

Fig. 4 Schematic illustration of the SERS measurement using an AgNP cluster based on SAW[92](A), the device based on NAEBs and equipped with a flow cytometry chip for detecting stem cells, along with the Raman test results[93](B), the BzBMN probe enhances Raman signals through enzyme-controlled aggregation-induced mechanism[94](C), utilizing the formation of aggregates for targeted enzyme-selective *in vitro* imaging of the tissue[95](D)

(A) Copyright 2024, Elsevier; (B) Copyright 2025, Elsevier; (C) Copyright 2025, American Chemical Society; (D) Copyright 2023, American Chemical Society.

For the molecular probe, aggregation-induced signal activation mechanisms demonstrate the deep integration of molecular design and Raman imaging. The BzBMN probe developed by Okinaka *et al.*[94] regulates molecular hydrophilicity/hydrophobicity through enzymatic hydrolysis, converting the originally dispersed hydrophilic substrate into a hydrophobic product that spontaneously aggregates in physiological environments. This process increases the local dye concentration by tens of times, leading to a linear enhancement in SRS signal intensity, and the aggregation kinetics are directly correlated with enzyme activity [Fig.4(C)]. This enzyme-controlled molecular aggregation overcomes the photobleaching limitations of traditional fluorescent probes. Utilizing the narrow peak characteristics of the cyano group in the cellular silent region with a full width at half maximum less than 10 cm^{-1} and employing isotope editing with $^{13}C/^{15}N$, simultaneous imaging of GGT and DPP4 enzyme activities is achieved with signal crosstalk less than 5% [Fig.4(D)][95]. The programmability of molecular aggregates provides a modular platform for multiplexed

biomarker detection, offering sensitivity at the single-cell level. Furthermore, the probes exhibit minimal leakage after aggregation, significantly improving the spatial fidelity of *in vivo* imaging.

The anisotropic aggregation of Janus-type Au-Ag heterostructures reveals a new mechanism of multi-component synergistic enhancement. Wang *et al.*[96] utilized Se-WCDs to reduce Au cores, followed by the directional growth of Ag islands on the surface, forming Janus particles rich in edges and nanogaps. When Hg^{2+} catalyzes the formation of Au-Ag@Hg amalgam, particles selectively aggregate *via* metallic bond bridging, increasing in size from 84.7 nm to 294.2 nm, with a ζ-potential change of −54.5 mV, resulting in a 44.5-fold enhancement of the 391 cm^{-1} peak for 4-ATP. This chemically driven specific aggregation not only generates electromagnetic-chemical synergistic enhancement with an enhancement factor up to 10^6, but also, due to FB1's coordination adsorption inhibiting aggregation, creates an "off" signal state, constructing an "on-off" sensing system. The intelligent responsiveness of the aggregates enables detection limits as low as 0.005 μg/L(Hg^{2+}) and 0.006 μg/L(FB1), far exceeding those of traditional SERS probes.

3.2 Development of AIE-Raman Dual-Modal Probes

AIE with Raman spectroscopy has catalyzed the development of a new generation of dual-modal probes, providing a full-scale solution from macroscopic screening to microscopic quantitative analysis for precision biomedical research. The core of this approach lies in the covalent integration of strong Raman reporter groups and AIEgens into a single probe architecture *via* molecular engineering, enabling the synergistic output of fluorescence and Raman signals. The AIE-SRS-Mito probe designed by Li *et al.*[97] is a typical example [Fig.5(A)]. By introducing a diphenylacetylene group into an α-cyanostilbene AIE scaffold, this probe not only retains its mitochondrial targeting capability but also generates a strong alkyne Raman peak at 2223 cm^{-1} in the cell-silent region, with fluorescence emission at 500 nm and a Stokes shift of 120 nm[Fig.5(B)]. Similarly, Jana *et al.*[98] coupled tetraphenylethylene(TPE) with an alkyne to construct a cationic probe 1, which demonstrated both fluorescence and SERS enhancement effects in imaging surface glycans on MDA-MB-231 breast cancer cells[Fig.5(C)]. The cyanosubstituted phenylene vinylene derivative R-1[Fig.5(D)] reported by Mishra *et al.*[99] achieved synchronous quenching and recovery of fluorescence and Raman signals through a CO_2-induced protonation-deprotonation assembly-disassembly mechanism. The poly strategy developed by Su *et al.*[100] is more systematic. By embedding diethylamino-modified TPE units into the conjugated backbone, the alkyne Raman signal of the resulting polymer CP0 was enhanced 17.1-fold compared to the standard EdU, while maintaining strong aggregated-state fluorescence at 630 nm[Fig.5(E)], clearly demonstrating the decisive role of molecular skeleton design on dual-modal performance. The key to this integration strategy lies in utilizing the twisted conformation of AIE molecules to suppress π-π stacking, ensuring high fluorescence efficiency in the aggregated state, while enhancing Raman polarizability through conjugated segments and avoiding functional interference between the two modalities.

The imaging advantages of dual-modal probes stem from the inherent complementarity of fluorescence and Raman techniques. The fluorescence channel, with its high sensitivity and rapid imaging capability, is suitable for dynamic tracking in live cells and macroscopic lesion localization. The "turn-on" mechanism of AIE molecules ensures strong fluorescence emission only after aggregate formation in target regions, resulting in extremely low background interference[97,100]. However, fluorescence intensity is susceptible to interference from microenvironmental polarity, viscosity, and cellular autofluorescence, limiting its quantitative accuracy. The Raman channel provides an ideal solution, as the signal in the cellular silent region of 1800—2800 cm^{-1} is free from background interference and exhibits high specificity to the vibration frequencies of chemical bonds. Li *et al.*[97] leveraged the linear concentration dependence of SRS (I_{SRS}=0.1567c, R^2=0.99944) to lower the detection limit to 8.5 μmol/L and precisely measured an intra-mitochondrial probe concentration as

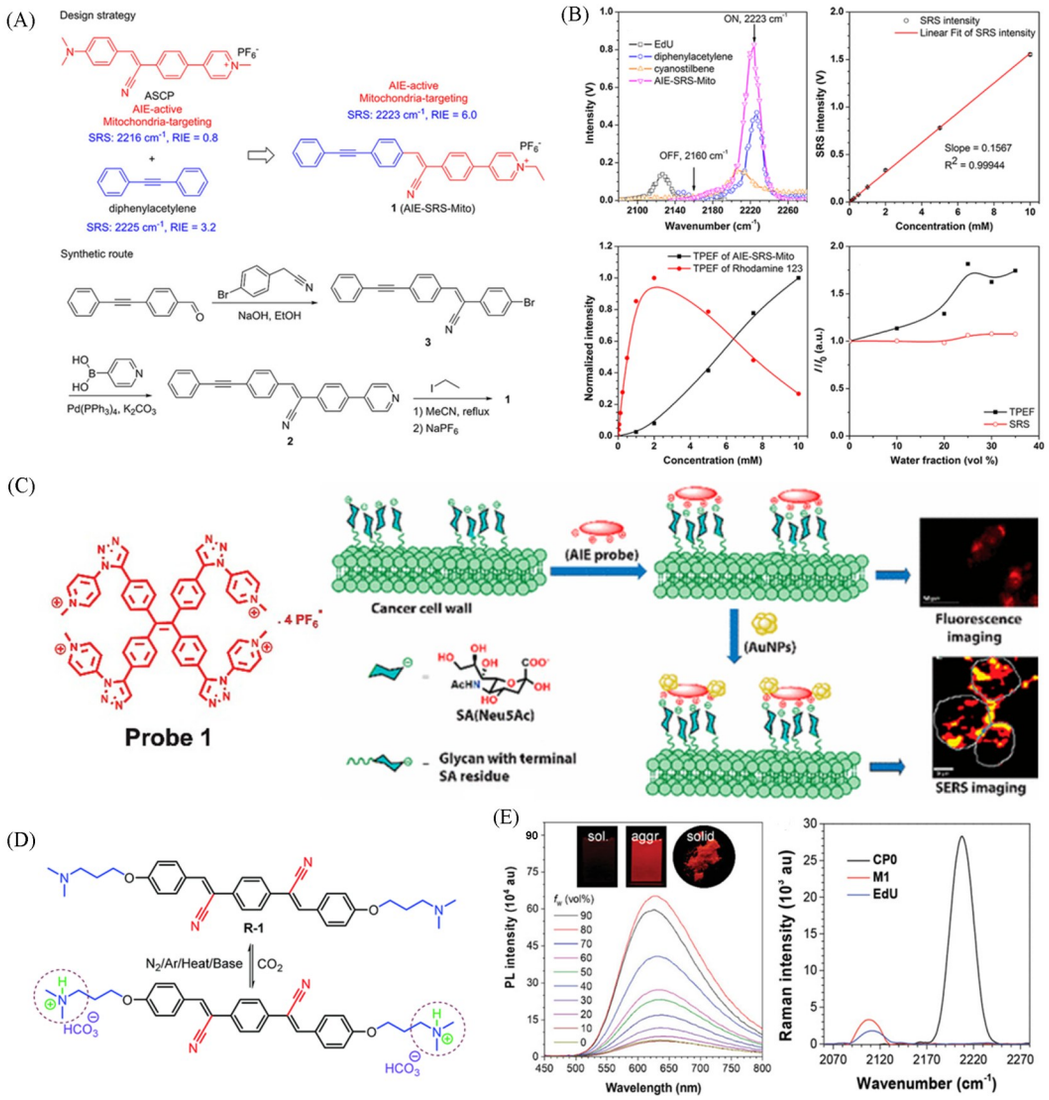

Fig. 5 Design Strategy and Synthetic Route of AIE-SRS-Mito[97](A), SRS and TPEF properties of AIE-SRS-Mito[97](B), the cell surface glycan imaging was achieved using the cationic probe 1 through fluorescence and SERS methods[98](C), receptor R-1 and its interaction with CO_2[99](D), the fluorescence and Raman properties of CP0[100](E)

(A) Copyright 2017, American Chemical Society; (B) Copyright 2023, American Chemical Society; (C) Copyright 2019, RSC; (D) Copyright 2021, Wiley-VCH.

high as 1.5 mmol/L, which is 75 times higher than the incubation concentration, achieving non-invasive quantitative mapping of AIEgens distribution in live cells for the first time. Su *et al.*[100] fully demonstrated this complementarity in tumor surgery navigation. The fluorescence signal from CP0 nanoparticles rapidly identified the main tumor mass, while the alkyne Raman signal precisely delineated the boundaries of residual lesions with micron-level resolution, guiding secondary resection until the signal disappeared. H&E staining verified the accuracy of Raman localization. This fluorescence localization-Raman quantification mode bridges the scale gap from macroscopic screening to microscopic verification.

3.3 AIEgen-Driven Specific Raman Sensing and Imaging

Organelle-specific imaging is an important application direction for AIE-Raman probes. The AIE-SRS-Mito probe designed by Li *et al.*[97] targets mitochondria *via* pyridinium cations, with perfect colocalization of fluorescence and SRS signals confirming its specific enrichment in the mitochondrial matrix[Fig.6(A) and (B)].

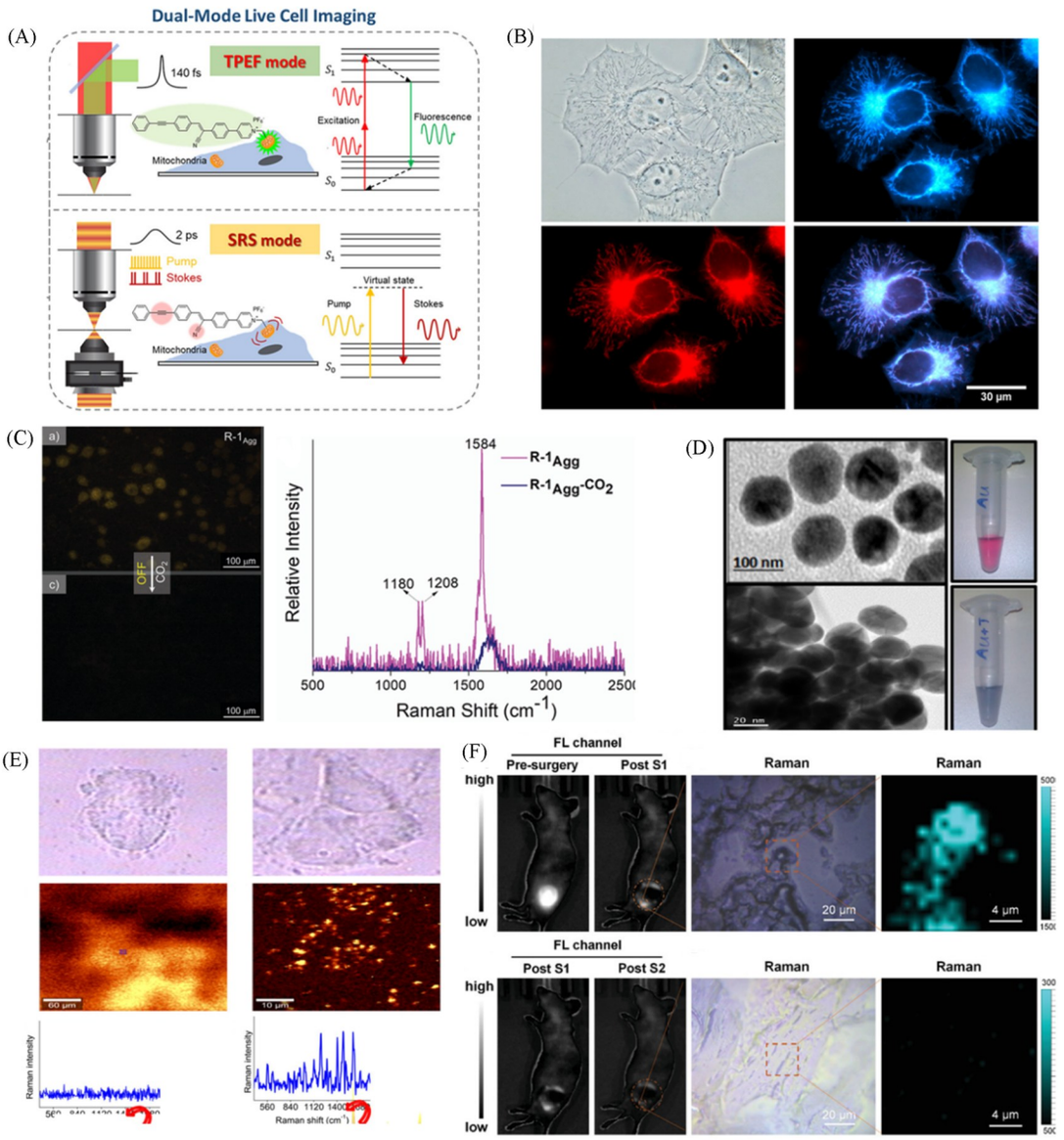

Fig. 6 Dual-mode live cell imaging using FL-SRS[97](A), Mitochondrial specificity of AIE-SRS-Mito[97](B), the R-1 aggregate exhibits reversible bimodal signal attenuation in response to changes in CO_2 concentration[99](C), TEM images of TPE-In-PSA@Au nanoprobe and corresponding visual color changes[101](D), Raman imaging of LNCaP and HeLa cells with TPE-In-PSA@Au nanoprobes[101](E), the tumor lesions of 4T1 tumor-bearing mice were fluorescently located and Raman cleared using CP0 nanoprobes[100](F)

(A, B) Copyright 2017, American Chemical Society; (C) Copyright 2019, RSC; (D, E) Copyright 2016, American Chemical Society; (F) Copyright 2021, Wiley-VCH.

This probe allows dynamic visualization of the mitochondrial reticulum, and *via* SRS quantification, reveals the transition of mitochondrial morphology from a tubular to a granular state under high-concentration incubation at 20 μmol/L for 105 min, a morphological change that directly correlates with cytotoxicity. This real-time monitoring of morphological changes provides a new method for studying organelle stress responses. Although lysosomal targeting has not been directly reported in the existing literature, the mechanism for the probe′s organelle selectivity has been validated, the charge density of cationic groups and differences in subcellular membrane potentials drive targeting specificity[97,100].

Regarding microenvironment-responsive imaging, the R-1 aggregates reported by Mishra *et al.*[99] exhibited reversible dual-modal signal attenuation in response to CO_2 concentration changes. In live A549

cells, when environmental CO_2 increased from 0.038% to 5%, fluorescence intensity decreased 25-fold, the average fluorescence lifetime shortened from 5.67 ns to 0.33 ns, and simultaneously the characteristic Raman peak at 1584 cm^{-1} disappeared[Fig.6(C)]. Dynamic light scattering confirmed a reduction in aggregate size from 156 nm to 83 nm, indicating that CO_2-induced protonation led to a hydrophobic-to-hydrophilic switch, triggering disassembly[99]. This pH-dependent response mechanism reveals the high sensitivity of AIE probes to microenvironmental acidification, offering potential for monitoring pathological processes like cellular metabolic acidosis.

Early cancer diagnosis and surgical margin delineation have been experimentally validated. The TPE-In-PSA@Au nanoprobe constructed by Maiti's team[101][Fig.6(D)], modified with PSA-specific peptides, achieved "signal-off" detection on the surface of LNCaP prostate cancer cells, specifically, the SERS signal attenuated after the peptide chain was cleaved by PSA protease, with the limit of detection(LOD) as low as 0.5 ng. In contrast, the signal remained stable in PSA-negative HeLa cells. SERS mapping clearly distinguished the two cell lines, providing single-cell resolution for liquid biopsy[Fig.6(E)]. The CP0 nanoparticle system developed by Su *et al.*[100] enabled rapid tumor localization *via* fluorescence in 4T1 tumor-bearing mice. Intraoperative Raman imaging identified residual lesions with micron-level precision, guiding secondary resection until the signal disappeared[Fig.6(F)]. Pathological analysis confirmed the technique's ability to detect sub-millimeter tumor fragments, significantly improving the negative surgical margin rate. Furthermore, the cationic polyelectrolyte CP2 reported in the same study demonstrated selective imaging and simultaneous killing capabilities against pathogens.

4 Challenges and Prospects

Certainly, the clinical translation of AIE-Raman dual-modal probes still faces multiple challenges. A primary concern lies with the commonly integrated metallic nano-substrates. Their long-term *in vivo* fate, metabolic pathways, organ-specific accumulation, and potential immunogenicity require thorough investigation, as highlighted by metabolomic studies on the chronic organ-specific toxicity of such nanomaterials[102]. For the AIEgens themselves, while often praised for excellent photostability, systematic evaluations under prolonged and intense irradiation relevant to clinical use are needed. More critically, the potential toxicity of their photodegradation products remains a significant yet under-explored biosafety issue crucial for long-term biocompatibility[103]. Regarding the integrated platform, research on AIE-Raman probes for biomarker detection is emerging, but their design and optimization for *in vivo* use are still at an early stage[104]. Crucially, comprehensive preclinical studies detailing pharmacokinetics, such as blood circulation half-life, biodistribution, and clearance pathways, along with systematic acute and chronic toxicity profiles, are scarce. Most current reports prioritize demonstrating imaging efficacy, with biosafety often limited to preliminary assessments. Therefore, advancing these dual-modal probes toward the clinic necessitates a major research shift to equally prioritize systematic pharmacology and toxicology studies alongside performance optimization. Secondly, the molecular engineering to construct compounds with both strong AIE and Raman activity is complex. Moreover, the excitation/detection conditions for fluorescence and Raman often conflict, making it difficult to establish a standardized platform. Additionally, imaging depth remains a limitation: scattering and absorption by biological tissues restrict the effective Raman imaging depth to about 1 mm, with signals sharply attenuating when extending into the second near-infrared window. Furthermore, the real-time analysis of massive spectral data and intelligent identification of disease biomarkers lack clinically validated and reliable AI models.

To address these current issues, researchers can focus on developing intelligent responsive probes,

designing signal-switching probes triggered by multiple tumor microenvironmental factors or other logical inputs to enhance signal-to-noise ratio and specificity. Deep integration of artificial intelligence technology can be pursued to construct data-driven models that integrate multi-dimensional data features for automatic tissue distribution recognition and treatment response prediction, while leveraging few-shot learning to tackle the scarcity of clinical data. Efforts can also be directed toward advancing second/third near-infrared window technologies, developing long-wavelength resonance Raman probes and dedicated hardware to capitalize on the low autofluorescence in these spectral regions, thereby achieving deeper, high signal-to-noise imaging. Furthermore, researchers may establish multi-modal fusion platforms that integrate the depth of photoacoustic imaging and the anatomical information from MRI, forming a cascaded strategy of macroscopic localization-microscopic verification. To accelerate clinical translation, scalable production processes can be established, promoting portable devices and standardized clinical trials, ultimately realizing the leap from laboratory innovation to clinical application.

5 Conclusions

The cross-integration of Raman imaging and AIE pioneers an innovative avenue to surmount the bottlenecks of traditional optical imaging. AIE molecules with aggregation-enhanced luminescence compensate for the intrinsic weak Raman signals, while Raman spectroscopy's molecular fingerprinting capability endows AIE probes with quantitative chemical information and unrivaled selectivity. Their synergy enables the "fluorescence localization-Raman quantification" mode to realize multiscale correlation and functional complementarity. This "1+1>2" strategy not only equips the imaging system with single-cell resolution, simultaneous multi-target detection and improved deep-tissue penetration, but also exhibits irreplaceable value in intraoperative tumor navigation, precision diagnosis and therapy of drug-resistant bacteria, and in vivo metabolic monitoring. With sustained breakthroughs in intelligent probe design, AI-driven data analysis and multimodal hardware integration, this integrative paradigm will propel biomedical imaging from structural observation to a new era of functional analysis and precise intervention, serving as a core technological bridge connecting fundamental research and clinical translation.

References

[1] Esteban R., Baumberg J. J., Aizpurua J., *Acc. Chem. Res.*, **2022**, *55*(14), 1889—1899
[2] Shipp D. W., Sinjab F., Notingher I., *Adv. Opt. Photonics*, **2017**, *9*(2), 315—428
[3] Jones R. R., Hooper D. C., hang L., Wolverson D., Valev V. K., *Nanoscale Res. Lett.*, **2019**, *14*(1), 231
[4] Pisano F., Masmudi-Martín M., Andriani M. S., Cid E., Kazemzadeh M., Pisanello M., Balena A., Collard L., Parras T. J., Bianco M., Baena P., Tantussi F., Grande M., Sileo L., Gentile F., de Angelis F., de Vittorio M., Menendez de la Prida L., Valiente M., Pisanello F., *Nat. Methods*, **2025**, *22*(2), 371—379
[5] Zhu L., Li J., Pan J., Wu N., Xu Q., Zhou Q. Q., Wang Q., Han D., Wang Z., Xu Q., Liu X., Guo J., Wang J., Zhang Z., Wang Y., Cai H., Li Y., Pan H., Zhang L., Chen X., Lu G., *Adv. Sci.*, **2024**, *11*(36), 2401014
[6] Huang C. C., Hsu Z. H., Lai Y. S., *Trends Food Sci. Tech.*, **2021**, *116*, 525—532
[7] Song L., Li J., *Small*, **2025**, *21*(4), 2407787
[8] Zhang C., Aldana-Mendoza J. A., *J. Phys. Photon.*, **2021**, *3*(3), 032002
[9] Zheng Y., Tan H., Jacobsen A., Liu Y., Ye C., Zhao Y., Xiang C., Yvind K., Pu M., *Laser Photonics Rev.*, **2025**, e02237, https://doi.org/10.1002/lpor.202502237
[10] Xu Q., Ding N., Ma D., Lin H., Lin B., Ma X., Yang J., Guo L., *Anal. Chem.*, **2024**, *96*(30), 12217—12224.
[11] Zhang Y., Gu Y., He J., Thackray B. D., Ye J., *Nat. Commun.*, **2019**, *10*(1), 3905
[12] Dodo K., Tipping W. J., Yamakoshi H., Egoshi S., Kubo T., Kumamoto Y., Faulds K., Graham D., Fujita K., Sodeoka M., *Nat. Rev. Methods Prim.*, **2025**, *5*(1), 20
[13] Siddhanta S., Kuzmin A. N., Pliss A., Baev A. S., Khare S. K., Chowdhury P. K., Ganguli A. K., Prasad P. N., *Adv. Opt. Photonics*, **2023**, *15*(2), 318—384
[14] Wang S., Liang Z., Gong Y., Yin Y., Wang K., He Q., Wang Z., Bai J., *J. Photoch. Photobio. B*, **2016**, *163*, 177—184

[15] Li Y., Shen R., Wu H., Yu L., Wang Z., Wang D., *Spectrochim. Acta Part A: Molecular and Biomolecular Spectroscopy*, **2020**, *225*, 117483
[16] Surmacki J. M., Sergot K., *Spectrochim. Acta Part A: Molecular and Biomolecular Spectroscopy*, **2026**, *347*, 126954
[17] Jang H., Li Y., Fung A. A., Bagheri P., Hoang K., Skowronska-Krawczyk D., Chen X., Wu J. Y., Bintu B., Shi L., *Nat. Methods*, **2023**, *20*(3), 448—458
[18] Shi L., Li Y., Li Z., *Light: Sci. Appl.*, **2023**, *12*(1), 234
[19] Abedin S., Li Y., Sifat A. A., Roy K., Potma E. O., *Nano Lett.*, **2022**, *22*(16), 6685—6691
[20] Zhitnitsky A., Benjamin E., Bitton O., Oron D., *Nat. Commun.*, **2024**, *15*(1), 10073
[21] de la Cadena A., Vernuccio F., Ragni A., Sciortino G., Vanna R., Ferrante C., Pediconi N., Valensise C., Genchi L., Laptenok S. P., Doni A., Erreni M., Scopigno T., Liberale C., Ferrari G., Sampietro M., Cerullo G., Polli D., *APL Photonics*, **2022**, *7*(7), 076104
[22] Zhang Y., Deng X., Wang S., Zhou W., Wu Z., Tang X., Lee H. J., Zhang D., *Angew. Chem. Int. Ed.*, **2025**, *64*(32), e202505038
[23] Song R., Yin X., Zhu M., Chen X., Zhang Z., Lyu X., Jiang S., Liu Z., Li Y., Zhang Z., Ban T., Li Y., *VIEW*, **2025**, *6*(4), 20240146
[24] Wang M., Zhang C., Yan S., Chen T., Fang H., Yuan X., *ACS Photonics*, **2021**, *8*(6), 1801—1809
[25] Pandya R., Dorchies F., Romanin D., Lemineur J. F., Kanoufi F., Gigan S., Chin A. W., de Aguiar H. B., Grimaud A., *Nat. Commun.*, **2024**, *15*(1), 8362
[26] Hu C., Wang X., Liu L., Fu C., Chu K., Smith Z. J., *Analyst*, **2021**, *146*(7), 2348—2357
[27] Zhou Q., Zou Z., Han L., *Coatings*, **2022**, *12*(8), 1229
[28] Zhang T., Li Y., Lv X., Jiang S., Jiang S., Sun Z., Zhang M., Li Y., *Adv. Funct. Mater.*, **2024**, *34*(17), 2315668
[29] Haque M. I. U., Lebron A., Alvarez F. J. D., Neal J. F., Mamak M., Mukherjee D., Ovchinnikova O. S., Hinkle J. D., *Appl. Phys. Lett.*, **2024**, *125*(20), 204104
[30] Wang X., Hu C., Chu K., Smith Z. J., *Analyst*, **2020**, *145*(20), 6607—6616
[31] Zhou Y., Zhang Y., Xie H., Wu Z., Shi B., Lin L. L., Ye J., *ACS Nano*, **2024**, *18*(52), 35393—35404
[32] Camp Jr C. H., Lee Y. J., Heddleston J. M., Hartshorn C. M., Walker A. R. H., Rich J. N., Lathia J. D., Cicerone M. T., *Nat. Photonics*, **2014**, *8*(8), 627—634
[33] Zhu W., Wang J., Lei K., Yan X., Xu J., Liu S., Li C., *Biosens. Bioelectron.*, **2025**, *271*, 116953
[34] Luo J. D., Xie Z. L., Lam J. W. Y., Cheng L., Chen H. Y., Qiu C. F., Kwok H. S., Zhan X. W., Liu Y. Q., Zhu D. B., Tang B. Z., *Chem. Commun.*, **2001**, (18), 1740—1741
[35] Zhang Q., Zhang Z., Liu J., Song A., Li C., Yang X., Zhang D., Ye Y., *Coord. Chem. Rev.*, **2026**, *547*, 217122
[36] Wu B., Shen J., Wang W., Xue T., He Y., *Dyes Pigments*, **2019**, *170*, 107569
[37] Baroni N., Turshatov A., Adams M., Dolgopolova E. A., Schlisske S., Hernandez-Sosa G., Wöll C., Shustova N. B., Richards B. S., Howard I. A., *ACS Appl. Mater. Interfaces*, **2018**, *10*(30), 25754—25762
[38] Rana S., Nayak S. R., Patel S., Vaidyanathan S., *J. Mater. Chem. C*, **2024**, *12* (3), 765—818
[39] Blas-Gómez S., Alonso-Moreno C., Garzón-Ruiz A., Bravo I., *Innovation*, **2025**, 101081, https://doi.org/10.1016/j.xinn.2025.101081
[40] Chen S., Wang H., Hong Y., Tang B. Z., *Mater. Horiz.*, **2016**, *3*(4), 283—293
[41] Zhang W., Cheng Y., Xu B., Luo Y., Su X., Zhou J., Wang X., Wu T., Chen N., Qiu H., Wu X., Xie L., *Dyes Pigments*, **2025**, *239*, 112750
[42] Petdee S., Arunlimsawat S., Itsoponpan T., Rueantong K., Saenubol A., Janthakit P., Nalaoh P., Sudyoadsuk T., Promarak V., *Opt. Mater.*, **2024**, *157*, 116413
[43] Zhang W., Kong J., Miao R., Song H., Ma Y., Zhou M., Fang Y., *Adv. Funct. Mater.*, **2024**, *34*(7), 2311404
[44] Gadiyaram S., Ghosh A., Ghule V. D., Sharma P. K., Amilan J. D., *Microchem. J.*, **2024**, *204*, 110957
[45] Khan I. M., Niazi S., Iqbal Khan M. K., Pasha I., Mohsin A., Haider J., Iqbal M. W., Rehman A., Yue L., Wang Z., *TrAC Trends in Analytical Chemistry (TrAC)*, **2019**, *119*, 115637
[46] Situ B., Ye X., Zhao Q., Mai L., Huang Y., Wang S., Chen J., Li B., He B., Zhang Y., Zou J., Tang B. Z., Pan X., Zheng L., *Adv. Sci.*, **2020**, *7*(4), 1902760
[47] Song S., Wang Y., Zhao Y., Huang W., Zhang F., Zhu S., Wu Q., Fu S., Tang B. Z., Wang D., *Matter*, **2022**, *5*(9), 2847—2863
[48] Yang Q., Wu Y., Chen J., Lu M., Wang X., Zhang Z., Xiong H., Choo J., Chen L., *Coord. Chem. Rev.*, **2024**, *507*, 215768
[49] Bao Y., Guo L., Gao Z., Yan Y., Duan Y., Zhao Y., Wang H., Xiao C., *Anal. Chem.*, **2025**, *97*(51), 28111—28123
[50] Wang N., Cao H., Wang L., Ren F., Zeng Q., Xu X., Liang J., Zhan Y., Chen X., *Curr. Med. Chem.*, **2020**, *27*(36), 6188—6207
[51] Kamei K. I. F., Wakamoto Y., *Microscopy*, **2025**, *74*(3), 189—200
[52] Hobro A. J., Smith N. I., *Vib. Spectrosc.*, **2024**, *131*, 103668
[53] Ando J., Palonpon A. F., Sodeoka M., Fujita K., *Curr. Opin. Chem. Biol.*, **2016**, *33*, 16—24
[54] Verduijn J., Degroote E., Skirtach A. G., *Commun. Biol.*, **2025**, *8*(1), 218
[55] Lazzini G., Gaeta R., Pollina L. E., Comandatore A., Furbetta N., Morelli L., D'Acunto M., *Sci. Rep.*, **2025**, *15*(1), 13240
[56] Ma R., Zhou L., Jiang S., Zhao X., Ma R., Sun J., Xia L., Liu X., Wang X., Meng Q., Yu H., Li Y., *Anal. Chem.*, **2025**, *97*(13), 7378—7387

[57] Sacharz J., Wrona E., Zięba-Palus J., Lewandowski M. H., Palus-Chramiec K., Chrobok Ł., Birczyńska-Zych M., Phan W., Wesełucha-Birczyńska A., *J. Mol. Struct.*, **2025**, *1348*, 143396
[58] Liu K., Ullah A. K. M. A., Juhong A., Yang C. W., Yao C. Y., Li X., Bumpers H. L., Qiu Z., Huang X., *Small Sci.*, **2024**, *4*(5), 2300154
[59] Chang H., Hur W., Kang H., Jun B. H., *Light: Science & Applications*, **2025**, *14*(1), 79
[60] Chen B., Gao J., Sun H., Chen Z., Qiu X., *Methods*, **2025**, *241*, 67—93
[61] Kim J., Kim J. M., Choi K., Park J. E., Nam J. M., *J. Am. Chem. Soc.*, **2024**, *146* (20), 14012—14021
[62] Lian S., Gao X., Song C., Li H., Lin J., *Langmuir*, **2021**, *37*(44), 12907—12918
[63] He C., Jiang L., Shi X., Zhuo Y., Yuan R., Yang X., *Anal. Chim. Acta*, **2025**, *1339*, 343604
[64] Yu J. H., Steinberg I., Davis R. M., Malkovskiy A. V., Zlitni A., Radzyminski R. K., Jung K. O., Chung D. T., Curet L. D., D'Souza A. L., Chang E., Rosenberg J., Campbell J., Frostig H., Park S. M., Pratx G., Levin C., Gambhir S. S., *ACS Nano*, **2021**, *15*(12), 19956—19969
[65] Harmsen S., Wall M. A., Huang R., Kircher M. F., *Nat. Protoc.*, **2017**, *12*(7), 1400—1414
[66] Qian X., Peng X. H., Ansari D. O., Yin-Goen Q., Chen G. Z., Shin D. M., Yang L., Young A. N., Wang M. D., Nie S., *Nat. Biotechnol.*, **2008**, *26*(1), 83—90
[67] Harmsen S., Huang R., Wall M. A., Karabeber H., Samii J. M., Spaliviero M., White J. R., Monette S., O'Connor R., Pitter K. L., Sastra S. A., Saborowski M., Holland E. C., Singer S., Olive K. P., Lowe S. W., Blasberg R. G., Kircher M. F., *Sci. Transl. Med.*, **2015**, *7*(271), 271ra7
[68] Yang Y., Zhu J., Weng G. J., Li J. J., Zhao J. W., *Chem. Eng. J.*, **2021**, *409*, 128173
[69] Zhang Q. H., Liu K., Qin K., Fu S. J., Du J., Lu Y. Q., Zhu Y. Y., Chen Y. F., Zhang X. J., *Physical Review Lett.*, **2025**, *134*(13), 136902
[70] Li M., Qiu Y., Fan C., Cui K., Zhang Y., Xiao Z., *Acta Pharmaceutica Sinica B*, **2018**, *8*(3), 381—389
[71] Samanta A., Maiti K. K., Soh K. S., Liao X., Vendrell M., Dinish U. S., Yun S. W., Bhuvaneswari R., Kim H., Rautela S., Chung J., Olivo M., Chang, Y. T., *Angew. Chem. Int. Ed.*, **2011**, *50*(27), 6089—6092
[72] Tian S., Li H., Li Z., Tang H., Yin M., Chen Y., Wang S., Gao Y., Yang X., Meng F., Lauher J. W., Wang P., Luo L., *Nat. Commun.*, **2020**, *11*(1), 81
[73] Chen M., Zhang L., Gao M., Zhang X., *Talanta*, **2017**, *172*, 176—181
[74] Zhang Y. Y., Tian S. D., Huang L. P., Li Y. A., Lu Y., Li H. Y., Chen G. P., Meng F. L., Liu G. L., Yang X. L., Tu J. S., Sun C. M., Luo L., *Nat. Commun.*, **2022**, *13*(1), 4553
[75] Zhao L., Cao Y., Xin Y., Liu C., Yang J., Li Y., Tian S., Liu Z., Jia H., Liu M., Hu M., Luo L., Meng F., *Small*, **2025**, *21*(13), e2411419
[76] Ge K., Ni R., Tao P., Zhao X., Luo Y., Zhu Y., Song B., Zhang W., Dai S., Zhang N., Xu T., Zhang P., *Opt. Commun.*, **2024**, *554*, 130183
[77] Jeong S., Kim Y. I., Kang H., Kim G., Cha M. G., Chang H., Jung K. O., Kim Y. H., Jun B. H., Hwang, D. W., Lee Y. S., Youn H., Lee Y. S., Kang K. W., Lee D. S., Jeong D. H., *Sci. Rep.*, **2015**, *5*(1), 9455
[78] Zhao J., Chen Y., Tang Y., Li B., Wang Q., Wang J., Gao X., Zhang Y., Wang J., Lei Z., Li C., Wang C., *Angew. Chem. Int. Ed.*, **2025**, *64*(25), e202504822
[79] Heiner Z., Gühlke M., Živanović V., Madzharova F., Kneipp J., *Nanoscale*, **2017**, *9*(23), 8024—8032
[80] Gao C., Lin W., Wang J., Wang R., Wang J., *Plasmonics*, **2018**, *13*(4), 1343—1358
[81] Jorio A., Nadas R., Pereira A. G., Rabelo C., Gadelha A. C., Vasconcelos T. L., Zhang W., Miyata Y., Saito R., Costa M. D. D., Cançado L. G., *2D Materials*, **2024**, *11*(3), 033003
[82] Hwang J., Jhe W., *Jpn. J. Appl. Phys.*, **2025**, *64*(4), 040801
[83] Zenobi R.. Kumar N., Verma P., *Nano Lett.*, **2025**, *25*(10), 3707—3716
[84] Mrđenović D., Ge W., Kumar N., Zenobi R., *Angew. Chem. Int. Ed.*, **2022**, *61*(43), e202210288
[85] Bakhtbidar M., Gueckelhorn D., Fernández-Serra M., López Y. L. L., Merlen A., Ruediger A., *Adv. Mater. Interfaces*, **2025**, *12*(11), 2401024
[86] Bi X., Czajkowsky D. M., Shao Z., Ye J., *Nature*, **2024**, *628*(8009), 771—775
[87] Chen C., Wang Y., Wu F., Hong W., *Anal. Chem.*, **2023**, *95*(42), 15556—15565
[88] Gupta S., Singh R., Bhardwaj S., Kuzmin A., Thakkur S., Garg S., Rzhevskii A., Vaitla J., Baev A., Siddhanta S., Prasad P. N., *ACS Photonics*, **2025**, *12*(9), 5074—5086
[89] Gu Y., Bi X., Ye J., *J. Mater. Chem. B*, **2020**, *8*(31), 6944—6955
[90] Li W., Yang L., Yin Y., Xu H., Li S., Xu J., Liu G., Gao H., Liu D., *Angew. Chem. Int. Ed.*, **2025**, *64*(46), e202509898
[91] Tang Y., Chen X., Zhang S., Smith Z. J., Gao T., *Anal. Chem.*, **2021**, *93*(47), 15659—15666
[92] Park J. O., Choi Y., Ahn H. M., Lee C. K., Chun H., Park Y. M., Kim K. B., *Anal. Chim. Acta*, **2024**, *1285*, 342036
[93] Fong Z. H., Wang C. H., Yang C. Y., Kan H. C., Lin Y. J., Chen Y. L., Shen Y. C., Yu Y. C., Chau L. K., Io C. W., Wang S. C., *Microchem. J.*, **2025**, *212*, 113436

[94] Okinaka M., Kawatani M., Fujioka H., Spratt S. J., Ito H., Misawa Y., Otake R., Ishikawa A., Kojima R., Urano Y., Ozeki Y., Kamiya M., *Anal. Chem.*, **2025**, *97*(35), 19057—19065
[95] Fujioka H., Kawatani M., Spratt S. J., Komazawa A., Misawa Y., Shou J., Mizuguchi T., Kosakamoto H., Kojima R., Urano Y., Obata F., Ozeki Y., Kamiya M., *J. Am. Chem. Soc.*, **2023**, *145*(16), 8871—8881
[96] Wang Y., Liang X., Yang Y., *Microchim. Acta*, **2025**, *192*(3), 172
[97] Li X., Jiang M., Lam J. W. Y., Tang B. Z., Qu J. Y., *J. Am. Chem. Soc.*, **2017**, *139*(47), 17022—17030.
[98] Jana P., Koppayithodi S., Murali M., Saha M., Maiti K. K., Bandyopadhyay S., *ACS Sensors*, **2023**, *8*(4), 1693—1699
[99] Mishra R. K., Vijayakumar S., Mal A., Karunakaran V., Janardhanan J. C., Maiti K. K., Praveen V. K., *Chem. Commun.*, **2019**, *55*(43), 6046—6049
[100] Su X., Liu R., Li Y., Han T., Zhang Z., Niu N., Kang M., Fu S., Wang D., Wang D., Tang B. Z., *Adv. Healthc. Mater.*, **2021**, *10*(24), 2101167
[101] Ramya A. N., Joseph M. M., Nair J. B., Karunakaran V., Narayanan N., Maiti K. K., *ACS Appl. Mater. Interfaces*, **2016**, *8*(16), 10220—10225
[102] Wang X., Ma Y., Wang C., Yang L., Wei S., Miao A., *Sci. Total Environ.*, **2025**, *1003*, 180708
[103] He W., Zhang T., Bai H., Kwok R. T. K., Lam J. W. Y., Tang B. Z., *Adv. Healthc. Mater.*, **2021**, *10*(24), 2101055
[104] Guan R., Yu Q., Li J., *Methods*, **2023**, *216*, 11—20

(Ed.: F, K, V)